Adjustable and robust methods for polarization-dependent focusing

David Schmid,[1*] Ting-Yu Huang,[1,2] Shiraz Hazrat,[1,3] Radhika Dirks,[1,4] Onur Hosten,[1,5] Stephan Quint,[1,6] Dickson Thian,[1,7] and Paul G. Kwiat[1]

[1]*Department of Physics, University of Illinois at Urbana-Champaign, 1110 W Green St, Urbana, IL 61801*
[2]*Department of Photonics, National Chiao Tung University, 1001 University St, Hisnchu, Taiwan*
[3]*Corporate Engineering, Google Inc., 201 S. Division St Suite 500, Ann Arbor, MI 48104, USA*
[4]*Shell Technology Ventures, Bellaire Technology Center, 3737 Bellaire Boulevard, Houston, TX 77025, USA*
[5]*Physics Department, Stanford University, 382 Via Pueblo Mall, Stanford, CA 94305, USA*
[6]*Institute for Applied Physics, TU Darmstadt, Schlossgartenstrasse 7, Darmstadt 64289, Germany*
[7]*Department of Applied Physics, Stanford University, 348 Via Pueblo Mall, Stanford, CA 94305, USA*
*schmid8@illinois.edu

Abstract: We present two methods for the precise independent focusing of orthogonal linear polarizations of light at arbitrary relative locations. Our first scheme uses a displaced lens in a polarization Sagnac interferometer to provide adjustable longitudinal and lateral focal displacements via simple geometry; the second uses uniaxial crystals to achieve the same effect in a compact collinear setup. We develop the theoretical applications and limitations of our schemes, and provide experimental confirmation of our calculations.

©2013 Optical Society of America

OCIS codes: (260.1440) Birefringence; (220.1000) Aberration compensation; (260.5430) Polarization; (260.1180) Crystal optics.

References and links

1. E. Higurashi, R. Sawada, and T. Ito, "Optically induced angular alignment of birefringent micro-objects by linear polarization," Appl. Phys. Lett. **73**(21), 3034 (1998).
2. J. B. Lassiter, M. W. Knight, N. A. Mirin, and N. J. Halas, "Reshaping the plasmonic properties of an individual nanoparticle," Nano Lett. **9**(12), 4326–4332 (2009).
3. M. O. El-Shenawee, "Polarization dependence of plasmonic nanotoroid dimer antenna," Antennas and Wireless Propagation Letters, IEEE **9**, 463–466 (2010).
4. C. M. Dutta, T. A. Ali, D. W. Brandl, T. H. Park, and P. Nordlander, "Plasmonic properties of a metallic torus," J. Chem. Phys. **129**(8), 084706 (2008).
5. K. Bonin, B. Kourmanov, and T. Walker, "Light torque nanocontrol, nanomotors and nanorockers," Opt. Express **10**(19), 984–989 (2002).
6. A. A. Yanik, R. Adato, S. Erramilli, and H. Altug, "Hybridized nanocavities as single-polarized plasmonic antennas," Opt. Express **17**(23), 20900–20910 (2009).
7. R. Rangarajan, L. E. Vicent, A. B. U'Ren, and P. G. Kwiat, "A. B. U'Ren, and P. G. Kwiat, "Engineering an ideal indistinguishable photon-pair source for optical quantum information processing," J. Mod. Opt. **58**(3-4), 318–327 (2011).
8. L. E. Vicent, A. B. U'Ren, R. Rangarajan, C. I. Osorio, J. P. Torres, L. Zhang, and I. A. Walmsley, "Design of bright, fiber-coupled and fully factorable photon pair sources," New J. Phys. **12**(9), 093027 (2010).
9. W. S. Bakr, A. Peng, M. E. Tai, R. Ma, J. Simon, J. I. Gillen, S. Fölling, L. Pollet, and M. Greiner, "Probing the superfluid-to-Mott insulator transition at the single-atom level," Science **329**(5991), 547–550 (2010).
10. F. Kenny, D. Lara, O. G. Rodríguez-Herrera, and C. Dainty, "Complete polarization and phase control for focus-shaping in high-NA microscopy," Opt. Express **20**(13), 14015–14029 (2012).
11. S. Sanyal and A. Ghosh, "High tolerance to spherical aberrations and defects of focus with a birefringent lens," Appl. Opt. **41**(22), 4611–4619 (2002).
12. S. Sanyal, Y. Kawata, S. Mandal, and A. Ghosh, "High tolerance to off-axis aberrations with a birefringent lens," Opt. Eng. **43**(6), 1381–1386 (2004).
13. Y. Unno, "Point-spread function for a rotationally symmetric birefringent lens," J. Opt. Soc. Am. A **19**(4), 781–791 (2002).
14. H. Kikuta, K. Iwata, and H. Shimomura, "First-order aberration of a double-focus lens made of a uniaxial crystal," J. Opt. Soc. Am. A **9**(5), 814–819 (1992).

15. J. P. Lesso, A. J. Duncan, W. Sibbett, and M. J. Padgett, "Aberrations introduced by a lens made from a birefringent material," Appl. Opt. **39**(4), 592–598 (2000).
16. S. Sanyal, P. Bandyopadhayay, and A. Ghosh, "Vector wave imagery using a birefringent lens," Opt. Eng. **37**(2), 592–599 (1998).
17. M. Avendaño-Alejo and M. Rosete-Aguilar, "Paraxial theory for birefringent lenses," J. Opt. Soc. Am. A **22**(5), 881–891 (2005).
18. S. Sanyal and A. Ghosh, "High focal depth with a quasi-bifocus birefringent lens," Appl. Opt. **39**(14), 2321–2325 (2000).
19. X. Liu, X. Cai, S. Chang, and C. Grover, "Cemented doublet lens with an extended focal depth," Opt. Express **13**(2), 552–557 (2005).
20. R. Rangarajan. "Photonic sources and detectors for quantum information protocols: a trilogy in eight parts." Diss. University of Illinois, Urbana-Champaign, 2010. Web. July 2010.
22. We assume that each focal location could be anywhere within a Gaussian distribution with width equal to the error measured on the original data points (and centered about the measured value). We then calculate one million sets of simulated data, each set containing one value from the Gaussian distribution associated with each measured point. We then calculate the slope of each set, and the Gaussian width of the 1 million sets of slopes gives an accurate error value on our measured value of the slope.
22. To see this, one can find the necessary lens displacement d for a given application by comparing the final beam waist $w_{out,2} = \sqrt{[\lambda \alpha f_2{}^2/\pi(\alpha^2 + d^2)]}$ for two lenses with the final beam waist $w_{out,1} = \lambda f_1/\pi w$ for one lens. For example, assume we want to achieve a focal size β times smaller than that possible with a single lens, so that $\beta = w_{out,1}/w_{out,2}$. Solving this equality for d gives $d = \sqrt{[(\beta f_2)^2 - \alpha^2]}$. If, then, we wish to focus five times more tightly (i.e., the desired beam waist is 5 times smaller than it was with only one lens), then d will be greater than 50, well within the range of validity of our equations.
23. K. Yonezawa, Y. Kozawa, and S. Sato, "Focusing of radially and azimuthally polarized beams through a uniaxial crystal," J. Opt. Soc. Am. A **25**(2), 469–472 (2008).
24. R. Goldstein, *Electro-optic Devices in Review* (Lasers and Applications, 1986).
25. B. E. A. Saleh and M. C. Teich, *Beam Optics, in Fundamentals of Photonics* (John Wiley & Sons, 1991).

1. Introduction

As the field of nano-optics advances, it is becoming critical to have complete control over the temporal and spatial distribution of light, including its vector character (i.e., polarization), with applications ranging from optimizing coupling with nanophotonic devices like plasmonic antennas, to using tailored optical beams to drive microscopic motors [1–6]. Polarization-dependent focusing (PDF) refers to the general idea of simultaneously focusing orthogonal polarizations to spots at customizable longitudinal and transverse locations. Such a capability is useful, for example, in optimally pumping downconversion crystals to generate indistinguishable entangled photon pairs or for collection of these photons [7,8]. Similar capabilities could also be useful for individually addressing different spin states of atoms in neighboring sites of an optical lattice [9].

Ideally, one could arbitrarily control the polarization and phase of a beam's cross-sectional profile, enabling the creation of numerous useful focal fields [10]. In practice, this remains expensive, lossy, and imperfect, and requires a large setup involving multiple spatial light modulators. Another possibility is to fabricate a birefringent lens, though this is technically challenging, expensive, and in fact does not yield optimal results [11–17]. Specifically, known aberrations [14,15] distort the extraordinary beam beyond practical limits for focal separations outside the Rayleigh range [16,17]. Several similar experiments [18,19] did manage to increase a system's depth-of-focus, but only on the micron scale. In addition, birefringent lenses are not tunable and cannot provide lateral separations. The large amount of past work on this topic is further motivation for our research, which greatly extends the capabilities of polarization-dependent focusing and solves the beam aberrations present in birefringent lenses.

To achieve the same result with readily available optical elements, in the simplest case, one might imagine focusing light through a birefringent slab or beam displacer, so as to shift the extraordinary focus with respect to the ordinary focus (conceptually, sending the light through equal-thickness slabs with index n_e or n_o should seemingly simply lead to two longitudinal focal planes). This approach fails, however, as walk-off distorts the beam's spatial mode, leading to blurred beam waists and elongated focal spots. In fact, even without

walk-off, this method does not work due to different $n_e(\theta)$ for each of the spatially-variant input angles over the beam's profile [20]. Here we present two rather different schemes to achieve precise independent focusing control of two orthogonal polarization states. Our first scheme uses a Sagnac interferometer, while the second relies on uniaxial crystals.

2. Polarization Sagnac scheme for polarization-dependent focusing

2.1 General layout

To geometrically achieve PDF, one could use polarizing beam splitters in an unbalanced interferometer to send orthogonal polarizations along paths of different lengths after a focusing lens; however, this arrangement is non-optimal for any applications which require the two beams to have a stable coherent phase relationship. Our novel approach involves placing a lens offset from the center of the hypotenuse of a polarizing Sagnac interferometer (Fig. 1). The counterclockwise and clockwise beams from the polarizing beam splitter (PBS) trace the same routes, thus retaining the unusual stability and simplicity of a Sagnac, while allowing the ability to independently shift the focal planes of the incident horizontal (H) and vertical (V) polarized beams. Specifically, these horizontally and vertically polarized spots move apart by twice the lens translation from the geometric center of the Sagnac.
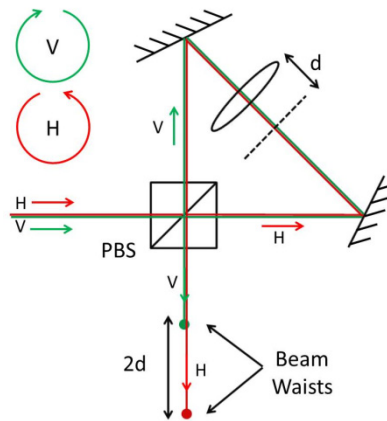

Fig. 1. Schematic of Sagnac with offset lens for focal separation along propagation axis.

2.2 Focal displacement along propagation axis

A Sagnac interferometer corresponding to Fig. 1 was set up with a 670-nm diode laser source. The laser output was first coupled to a single-mode fiber (SMF) to purify the spatial mode, and the 150-μW SMF output was then magnified to a collimated beam of radius of 2.2 mm. The focusing lens, placed inside the 150-mm hypotenuse of the Sagnac, had focal length of 400 mm, and was biconvex to keep aberrations symmetric (plano-convex lenses would be preferable, if only a single pass were used, but in our double-pass arrangement, the two directions would experience significantly different aberrations.). The focal plane of each polarization was separately measured by rotating the input polarization such that the beam took only one path at a time through the interferometer. For focal separations well outside the Rayleigh range, the defocused beam would have a negligible contribution to the focused power distribution. The measurement was taken by scanning a beam profiler (Thorlabs model BP104-VIS) along the propagation axis. All focal sizes and locations hereafter were found using this same method.

Focal separations (the distance from the focal plane of the H-polarized beam to the focal plane of the V-polarized beam) from 0.4 mm to 20 mm were measured; the focal separation versus lens displacement is plotted in Fig. 2. A linear fit shows that the theoretical slope of 2 is almost perfectly satisfied by our data with a slope of 2.003 ± 0.023. The error was

calculated using Monte Carlo simulated data [21].The beam waist at every sample point exhibited the desired Gaussian-mode profiles for both polarizations, with radii of around 38 μm (the theoretical diffraction limit is ~37 μm) indicating that any aberrations introduced by the extra optics are negligible. In section 2.4 we discuss methods for even tighter focusing.
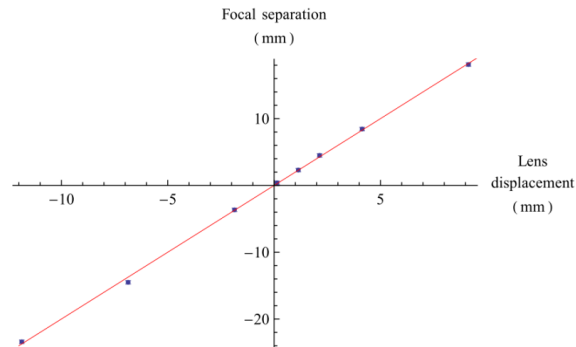

Fig. 2. No-free-parameter theory and experimental data for focal separation versus lens displacement. Vertical and horizontal error are negligible.

2.3 Lateral focal displacements

Another advantage of our geometric approach to PDF is that one can also induce *lateral* focal displacements simply by translating one of the mirrors. With an ideal thin lens, simple trigonometry shows that offsetting either of the mirrors by a distance d along the hypotenuse causes an expected transverse shift of $d/\sqrt{2}$, as illustrated in Fig. 3.

Experimental results for small lateral offsets in the range from −2 to 2 mm about the center of the mirror are shown in Fig. 4(a); the slope of the best-fit line for focal separation versus mirror offset was 0.706 ± 0.005; for larger mirror offsets ranging over 24 mm (Fig. 4(b)), the measured slope was 0.714 ± 0.006.
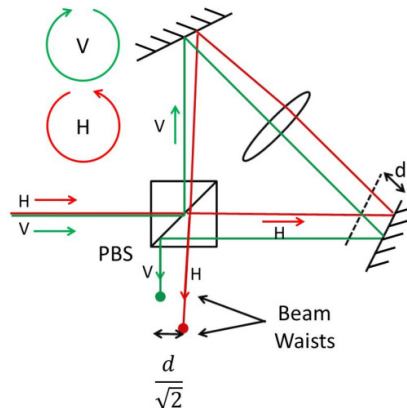

Fig. 3. Schematic of Sagnac setup for lateral focal separation induced by mirror offset. We show a large offset for illustration purposes. Note that a mirror translation induces both longitudinal and transverse separations; the ratio of these two effects can be tuned by changing the Sagnac geometry, specifically the deflection angle at the translating mirror.
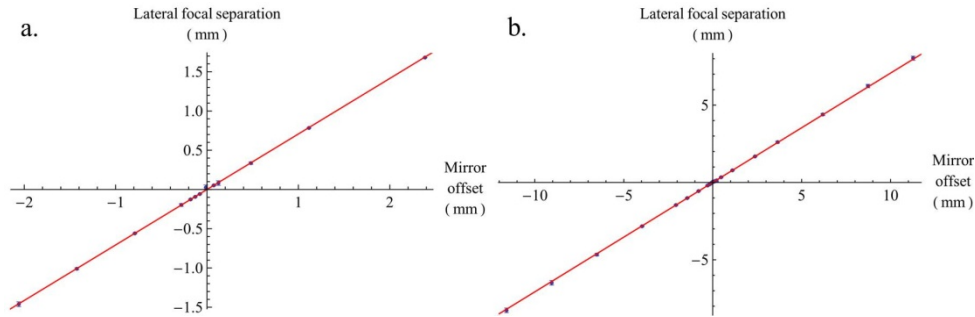
Fig. 4. Experimental data and theoretical slope of $1/\sqrt{2}$ for focal separation versus mirror offset for small offsets (a) and larger offsets (b). Vertical error bars are small but included; horizontal error is negligible (< 10 μm).

Here we note two further caveats. First, this lateral translation is also accompanied by a shift *along* the propagation axis $(1 + 1/\sqrt{2})d$. This does not pose a problem even if pure lateral displacement of the foci were desired, since such an effect can always be compensated by offsetting the lens as in Subsection 2.2. Second, since this scheme involves one beam hitting the lens off-center, the two orthogonal polarizations will be traveling in slightly different directions at the focus. This deviation will depend on the focal length of the lens and on the mirror offset, and will often be insignificant.

2.4 Two-lens scheme for tighter focusing

Some applications may require a much smaller waist radius, and therefore tighter focusing. Since the size of the Sagnac constrains the minimum focal length lens allowed in a setup such as Fig. 1, we considered a scheme using an additional lens outside the interferometer to achieve two equally sized, tightly focused, longitudinally separated focal points. While such a two-beam, two-lens system could in principle be quite complicated, we show in Appendix A that with the correct placement of the additional lens, the first lens (inside the Sagnac) may be translated to change the focal sizes and separation *with no further adjustments* to the second lens (outside the Sagnac).
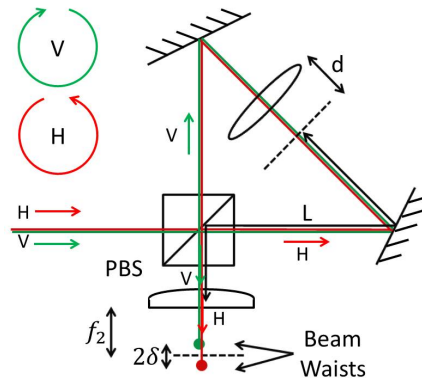

Fig. 5. Schematic of Sagnac for tighter focusing with two lenses.

To test this delightfully simple result, we placed a plano-convex lens with a focal length of 15 mm after the output port of the polarizing beam splitter, as shown in Fig. 5, and decreased the input beam radius to 1.7 mm for convenience of measurements. The lens after the Sagnac was then translated until the waist radii of the H- and V-polarized beams were identical to within measurement error, typically $\pm$ 0.2 μm; this lens was then kept at this location as the intra-interferometer lens was translated.

In Appendix A we derive the theoretical beam waist and focal separation versus lens translation. This derivation uses an approximation that will be valid for a large range of systems, giving a model for our two-lens setup as illustrated in Fig. 5. We find

$$\Delta = \frac{d f_2^2}{\alpha^2 + d^2} \tag{1}$$

$$w_{out} = \sqrt{\frac{\lambda \alpha f_2^2}{\pi(\alpha^2 + d^2)}} \tag{2}$$

$$\alpha \sim \frac{\lambda f_1^2}{\pi w^2}, \tag{3}$$

where Δ is the longitudinal displacement of either foci relative to a "pivot" point (a focal length f_2 away from the second lens); w_{out} is the beam waist of the foci; α is a constant determined by parameters of the setup; d is the displacement of the lens in the Sagnac from its center location (for $d = 0$ both polarizations focus to the same spot); f_1 and f_2 are the focal lengths of the first and second lens, respectively; λ is the wavelength; and w is the input beam radius. For our experiment, $f_1 = 400$ mm; $f_2 = 15$ mm; $\lambda = 670$ nm; and $w = 1.7$ mm; thus, α ~11.8 mm.

Because the lens could not be translated indefinitely inside our Sagnac without hitting another optical component, data points were impossible for d values from around 50 to 100 mm. However, data points from $d = -10$ to $d = 40$ mm (hereafter, range 1) were measured with the lens translating in the hypotenuse; and those for $d = 105$ to $d = 150$ mm (hereafter, range 2) were measured with the lens instead translating in one arm of the Sagnac. For both ranges 1 and 2, the absolute lens displacement value d was measured with respect to the geometric center of the Sagnac; the location of this central point could not be measured directly for range 2, and so was first extrapolated from the data using the single-lens setup and methods of Subsection 2.2.

The plots for Δ and w_{out} versus d are shown in Fig. 6(a) and 6(b), respectively. For large d values, the theoretical curves are followed closely in both plots; however, the Δ-versus-d data points deviate significantly from theory when d is smaller than 10. Since this deviation occurs only at *small* values of d, it is of minimal concern; the two-lens setup is only necessary when small spot sizes are required, which corresponds to *large* values of d, as seen in Fig. 6(b) [22].
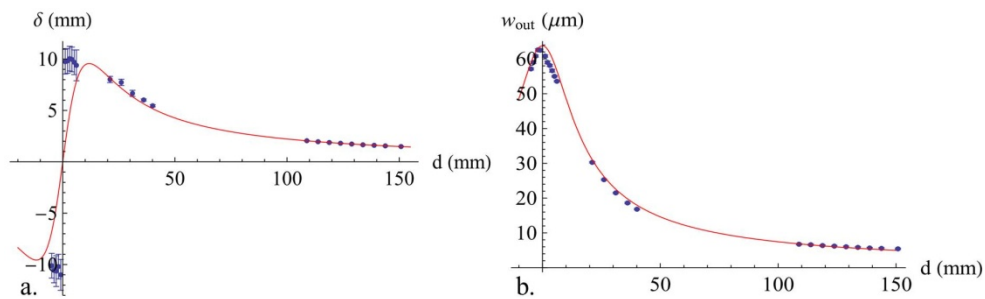

Fig. 6. (a). Data and fit for the focal separation Δ versus lens offset d; (b). data and fit for the beam waist w_{out} versus lens offset d. Horizontal error is again negligible (< 10 μm).

We note that this two-lens system is not as tunable as the single-lens system demonstrated in Subsection 2.2, since the beam sizes are dependent on the same parameters as the focal separation. However, this setup is nevertheless particularly useful when the desired

beam size is smaller than those reachable by a single lens with a finite aperture. The focal separations and focal sizes can then be tailored over a reasonable range using Eqs. (1)–(3).

3. Birefringent block focusing

3.1 One-crystal setup

Our Sagnac method for polarization-dependent focusing is highly customizable and allows for tunable longitudinal and transverse separations over a range from microns to millimeters. However, a collinear setup is often more desirable for its robustness, efficient use of space, ease of alignment, and potential for miniaturization. To this end, one could imagine focusing a beam through a birefringent crystal as in Fig. 7(a); then, the extraordinary beam H sees an index of refraction different from that of the ordinary beam V, resulting in different focal shifts, given by $\Delta = 1 - 1/n(\theta)$. However, in fact this equation does not hold, since the crystal induces a large astigmatism in the extraordinary beam, blurring out the focal plane by several times the desired focal separation, as suggested in [20].
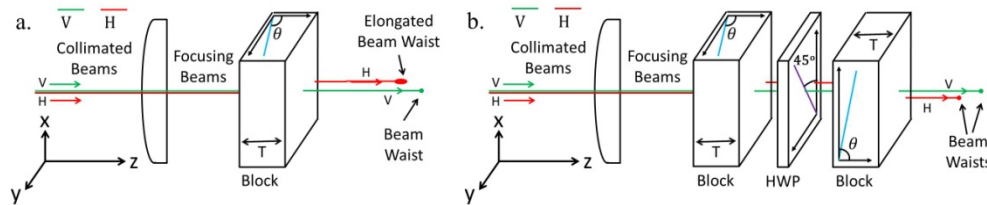

Fig. 7. (a). Schematic for one-block focusing; this model induces astigmatism. (b). Two-block setup for canceling aberrations; this model incurs additional lateral focal separations.

To demonstrate, consider focusing light through a 39.7-mm-long calcite crystal with optic axes at $\theta = 45°$ (arranged as in Fig. 7(a)) using a 200-mm focal length lens. For this configuration, calculations using Appendix B.3 show that the o-rays, e-rays in the x-z plane, and e-rays in the y-z plane all focus to different locations. This can be characterized by the theoretical values $\Delta z_{o,ex} = 1.11$ mm and $\Delta z_{o,ey} = 4.13$ mm, the distances from the two respective e-ray focal planes to the o-ray focal plane. Thus we see that the e-ray has gained a longitudinal astigmatism greater than the induced "focal separation", which is completely washed out. This result was tested experimentally by sending a laser beam ($\lambda = 702$ nm) with input radius 1.5 mm through the setup described above, and scanning the aforementioned beam profiler to find the focal locations, obtaining good agreement with theory: $\Delta z_{o,ex} = 1.17 \pm 0.15$ mm and $\Delta z_{o,ey} = 4.09 \pm 0.15$ mm. All data taken in Section 3 used the same measurement method, same input beam, and crystals with parameters identical to the above.

The manifestation of this astigmatism- an elongation of the beam radius along one axis-can be avoided only if the crystal's optic axis lies along the propagation axis. Unfortunately, in this case, the eigenmodes of the crystal are then, by symmetry, the radial and azimuthal polarization states [23], while the system's desired eigenmodes are H and V.

3.2 Two-crystal setup

The astigmatism induced from focusing through a crystal of arbitrary axis cut can be compensated for by propagating through a half-wave plate (HWP) and an identical crystal, rotated about the propagation axis by 90°, as seen in Fig. 7(b). (The HWPOHWP merely ensures that ordinary and extraordinary do not swap roles.) The system now becomes symmetric along the x- and y-axes, such that elongations in one crystal are inverted in the second crystal, and the beam leaves the setup with the desired symmetric cross-section. Having eliminated aberrations, we now turn to the relative focal locations produced in this two-crystal scheme, as calculated with the algorithm in Appendix B.

The dependence of the separation (per crystal length T) $\Delta z/T$ along the z-axis between the o-ray and e-ray focal planes versus optic axis angle θ (with respect to the surface normal) is shown in Fig. 8(a). We find that as θ increases from 0, Δz decreases monotonically until it reaches a constant small value (10's of microns) determined by the type and thickness of the crystals. Near $\theta = 0$, linear polarizations again no longer correspond to ordinary and extraordinary eigenmodes, and near $\theta = 90°$, the focal separation goes to zero. Thus, to achieve two separated, diffraction-limited H and V focal spots, one must use two crystals with an optic axis angle in between these two extremes. A potential limitation of this elegant solution is that in addition to focal separation, walk-off of the e-ray creates focal displacements along the x- and y-axes. These displacements, Δx and Δy, are on the same order of magnitude as the z-axis displacement Δz; see Fig. 8(b).
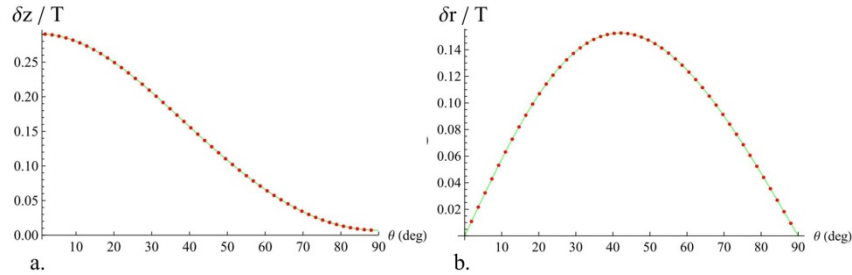

Fig. 8. Theoretical characterization of longitudinal focal separation (a) and lateral focal separation $\Delta r = \sqrt{[\Delta x^2 + \Delta y^2]}$ of ordinary and extraordinary spots (b) per crystal thickness T versus the optic axis angle θ for the two-block scheme shown in Fig. 7(b). For simplicity, the focal separations were calculated assuming the two input polarizations were ordinary and extraordinary, not necessarily horizontal and vertical (see text for discussion).

To test our aberration compensation model, we focused a laser ($\lambda = 702$ nm, $w = 1.5$ mm) through a HWP and two 39.7-mm-long calcite crystals with optic axes at $\theta = 45°$ (as in Fig. 7(b)) using a 200-mm focal length lens. Our algorithm predicts a theoretical focal separation of the H- and V-polarized spots of $\Delta z = 5.24$ mm and transverse separations of $\Delta x = \Delta y = 4.26$ mm. Experimental values for the separations Δz_x and Δz_y, with beam waists measured in the x-z and y-z planes, respectively, agreed with theory: $\Delta z_x = 5.26 \pm 0.15$ mm and $\Delta z_y = 5.14 \pm 0.15$ mm. Transverse separations were $\Delta x = 4.37 \pm 0.11$ and $\Delta y = 4.14 \pm 0.11$. The error was estimated by repeating the measurement multiple times after realigning the setup. Both focused beam waists were circular, and nearly diffraction limited, at just under 22 μm. The large astigmatism was thus successfully canceled, as seen in Fig. 9.

While repeating the experiment to find the measurement error, we noticed that changing the precise input position on each crystal altered the error significantly. The data given above was measured for a single set of crystals and orientations; by averaging data for various permutations, we found $\Delta z_x = 5.38 \pm 0.25$ mm and $\Delta z_y = 5.18 \pm 0.23$ mm. Although this agrees with our calculations, the increased variation in data could be problematic for practical applications. It is important to note that by translational symmetry, homogenous and identical crystals would only exhibit such a problem if mis-aligned, or given other imperfect components. We measured alignment tolerances and other potential sources of error, such as beam aberrations, beam clipping, crystal wedge, and cross-talk; none contributed significant error.
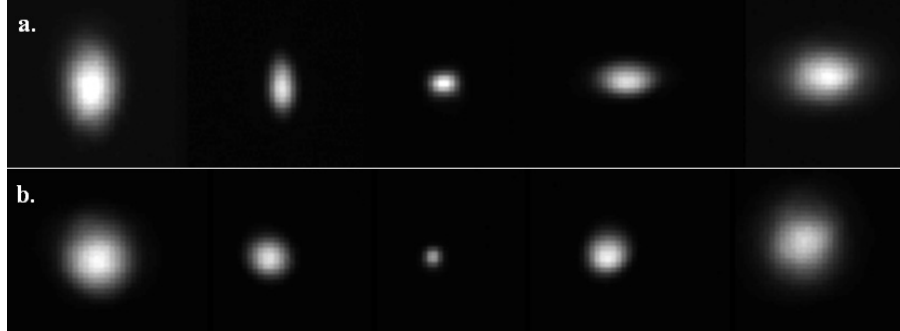
Fig. 9. Cross-sectional photographs of the extraordinary beam's intensity every 0.6 mm along the propagation axis of the laser. a.) Elliptical beam distortions (with maximum aspect ratio 2:1) are quite evident in the cross-sectional intensity profile of the extraordinary beam after focusing through 79.4 mm of calcite with optic axis at angle 45°. b.) The circular, un-aberrated profile is restored if the same focusing beam instead traverses two 39.7-mm blocks of calcite, oriented as in our compensation scheme.

Therefore, we suspect that small imperfections in the calcite itself were responsible for the variance in our data. This problem returns in our four-crystal setup, where the increased number of crystals increases the effect.

3.3 Four-crystal setup

If purely longitudinal focal displacements are necessary, we must finally compensate for the walk-off such that $\Delta x = \Delta y = 0$. We could accomplish this by mirror-reflecting the setup about the final crystal face, thus providing a Δz twice that of the two-block scheme, but now with the beam walking off-axis and then back. Rearranging allows us to use fewer waveplates; the most economical setup we found requires four birefringent blocks and one HWP, oriented as shown in Fig. 10. Both lateral and longitudinal displacements are proportional to crystal thickness, but the relative effects can be tuned by changing the optic axis cut. If an application is somewhat insensitive to transverse separations, then the simpler two-block scheme may suffice. (We note a superficial resemblance to four-crystal transverse field modulation in Pockels cells [24]; however, the basic idea and end product are entirely unrelated.)
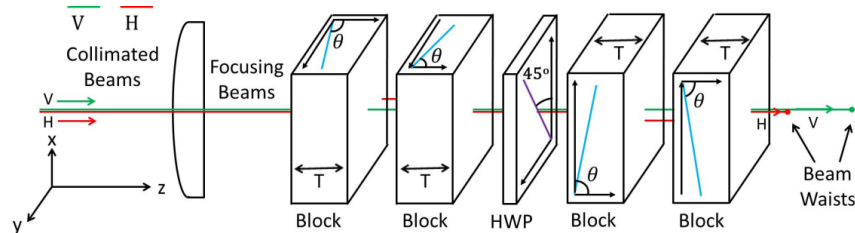

Fig. 10. Collinear, four-block setup for purely longitudinal, aberration-free focal displacements.

We tested this model using a lens with focal length 400 mm and the setup shown in Fig. 10, with the same beam and crystals specified above. For one specific input position, we found the values $\Delta z_x = 10.39 \pm 0.15$ mm and $\Delta z_y = 10.43 \pm 0.15$ mm, in good agreement with theory ($\Delta z = 10.48$ mm). However, we again observed data variation depending on the precise transverse crystal positions. Averaging over various input positions, we obtain the values $\Delta z_x = 10.73 \pm 0.37$ mm and $\Delta z_y = 10.80 \pm 0.68$ mm. The fairly large standard deviation of these measurements suggests the need for higher quality crystals; nonetheless, it is evident that this scheme for polarization-dependent focusing matches our calculations. The transverse separation went nearly to zero as expected, with $\Delta x = 6 \pm 7$ μm and $\Delta y = 9 \pm 7$ μm.

4. Conclusion

We have designed and demonstrated two schemes for achieving precise polarization-dependent focusing: a highly customizable method based on geometric path differences in a Sagnac interferometer, and a compact collinear method using birefringent crystals. Given a desired focal placement and waist size, one can determine which system is the most efficient, and then use it to control the relative focal locations of H and V in three dimensions. Simple modifications grant this scheme great flexibility. For example, if the desired eigenmodes were L and R, one could place two quarter-waveplates, one before our setup and one after, to achieve the same polarization-dependent focusing. As an added bonus, by varying the polarization angle of the input, one can automatically control the relative intensities of the two focal spots. One could also readily control the coherence between the two polarizations by using a tunable unbalanced interferometer (with polarizing beamsplitters), whose polarization-dependent path lengths may be adjusted outside the coherence length of the incident light. We envision the use of our techniques in polarization-sensitive optical-micromachining and plasmonic applications, as well as for shaping ideal sources and collection optics in quantum information processing.

Appendix A: Derivation of equations for two lenses

The following derivations use ABCD matrices for Gaussian beams using complex beam parameters under the thin-lens approximation [25]. We will derive the relation between the displacement of our intra-Sagnac lens and focal plane displacements about a pivot point, and the relation between this lens displacement and the final beam waist size.
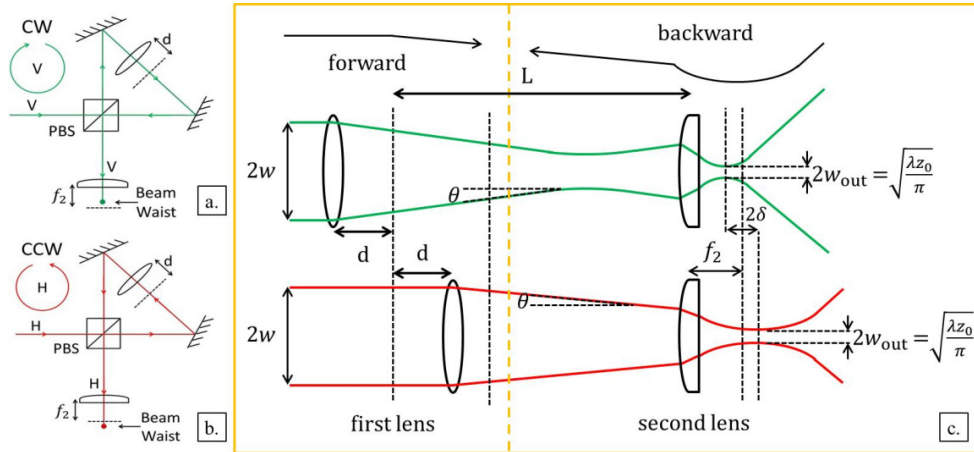

Fig. 11. Schematic of two Gaussian beams propagating through two lenses. The CW (a) and CCW (b) paths correspond to the collinear model of the same color displayed in (c). Our calculations for both of these paths are split into two parts, forward and backward, as shown with yellow boxes. Setting the forward and backward beams from the two calculations to have equal beam parameters at their intersection then provides our final result.

Because the mirrors and beamsplitters in our Sagnac (Fig. 5) merely redirect the beam without modification, we "collinearize" our setup (to simplify the calculation). We then effectively have two beams traveling through two lens systems, one beam corresponding to the clockwise (CW) path in the Sagnac; the other to the counterclockwise (CCW) path (as in Fig. 11). The only difference between the lens systems is that the first lens is offset in opposite directions by a distance d, as in Subsection 2.2. We require both the CW and CCW paths to have the same incident beam waist and the same output beam waist, but with focal plane locations differing by 2δ as labeled. We can split our calculation up into two parts, henceforth called "forward" and "backward". For the forward calculation, we trace the input beam of

waist w through the first lens and through free space to the second len's surface; in the backward calculation, we assume our target solution, two focal spots of the same radius separated by 2δ, and propagate these beams backwards through the second lens. Finally, we match the complex beam parameters of the two calculations at the second lens.

First, we calculate the backward propagation. Assuming our target solution gives us two Gaussian beams,

$$q_a = z_a + iz_0 \tag{4}$$

$$q_b = z_b + iz_0. \tag{5}$$

After propagating through the second lens, we require these beams to have identical divergence angles $\theta = \sqrt{[\lambda/(\pi\, z_0)]}$ and identical Rayleigh ranges z_0'. For an arbitrary optical element represented by an ABCD matrix we have [25]:

$$q' = z' + iz_0' = \frac{A + \dfrac{B}{q}}{C + \dfrac{D}{q}} = \frac{(Az + B) + iz_0 A}{(Cz + D) + iz_0 C} \tag{6}$$

$$z' = \mathrm{Re}[\frac{(Az + B) + iz_0 A}{(Cz + D) + iz_0 C}] = \frac{(Az + B)(Cz + D) + (z_0 A)(z_0 C)}{(Cz + D)^2 + (z_0 C)^2} \tag{7}$$

$$z_0' = \mathrm{Im}[\frac{(Az + B) + iz_0 A}{(Cz + D) + iz_0 C}] = z_0 \frac{A(Cz + D) - C(Az + B)}{(Cz + D)^2 + (z_0 C)^2}. \tag{8}$$

For a thin lens, A = 1, B = 0, C = −1/f, D = 1:

$$z' = \frac{z\left(1 - \dfrac{z}{f_2}\right) - \dfrac{z_0^2}{f_2}}{(1 - \dfrac{z}{f_2})^2 + (-\dfrac{z_0}{f_2})^2}; \qquad z_o' = \frac{z_0}{(1 - \dfrac{z}{f_2})^2 + (-\dfrac{z_0}{f_2})^2}. \tag{9}$$

To satisfy our condition of identical Rayleigh ranges,

$$z_{0a}' = \frac{z_0}{\left(1 - \dfrac{z_a}{f_2}\right)^2 + \left(-\dfrac{z_0}{f_2}\right)^2} = \frac{z_0}{\left(1 - \dfrac{z_b}{f_2}\right)^2 + \left(-\dfrac{z_0}{f_2}\right)^2} = z_{0b}' = z_0' \tag{10}$$

$$\left(1 - \frac{z_a}{f_2}\right) = \pm\left(1 - \frac{z_b}{f_2}\right) \rightarrow z_a = z_b \text{ or } z_a + z_b = 2f_2. \tag{11}$$

The second solution $z_a + z_b = 2f_2$ is the relevant equation. Thus, we can define $z_a \equiv z_+ = f_2 + \delta$; $z_a \equiv z_- = f_2 - \delta$ which then gives us

$$z_\pm' = f_2 \mp \frac{f_2^2 \delta}{\delta^2 + z_0^2}; \; z_{o\pm}' = z_0' = \frac{f_2^2 z_0}{\delta^2 + z_0^2}. \tag{12}$$

Next we carry out the forward calculation. Assuming that the input beam is collimated, then the Gaussian beam parameter for both polarizations will be $q_i = i\pi w^2/\lambda$, where $\pi w^2/\lambda = z_{0i}$ is the Rayleigh range. Focusing the beams through the first lens, we again use Eq. (9) to obtain:

$$z_i' = -\frac{(\pi w^2)^2 f_1}{(\lambda f_1)^2 + (\pi w^2)^2} = -\frac{\pi w^2 \alpha}{f_1} \tag{13}$$

$$z_{oi}' = \frac{\pi w^2 \lambda f_1^2}{(\lambda f_1)^2 + (\pi w^2)^2} \equiv \alpha. \tag{14}$$

Thus, the forward calculation gives the beam parameters $q_{i\pm}$ of the CW and CCW beams, respectively, at the second lens, as $q_{i\pm} = z_i' + L \pm d + iz_{0i}' = -\pi w^2 \alpha / f_1 + L \pm d + i\alpha$, where L is the distance from the center location of the first lens to the location of the second, d is the displacement of the first lens from its center location, and α is defined for convenience.

Now, we match the beam parameters from the forward and backward calculations:

$$-\frac{\pi w^2 \alpha}{\lambda f_1} + L \pm d + i\alpha = f_2 \pm \frac{f_2^2 \delta}{\delta^2 + z_0^2} + i\frac{f_2^2 z_0}{\delta^2 + z_0^2} \tag{15}$$

to obtain the following solutions:

$$L = f_2 + \frac{\pi w^2 \alpha}{\lambda f_1} \tag{16}$$

$$w_{out} = \sqrt{\frac{\lambda \alpha f_2^2}{\pi(\alpha^2 + d^2)}} = \sqrt{\frac{\lambda z_0^2}{\pi}} \tag{17}$$

$$\delta = \frac{df_2^2}{\alpha^2 + d^2} \tag{18}$$

$$\alpha = \frac{\pi w^2 \lambda f_1^2}{(\pi w^2)^2 + (\lambda f_1)^2}. \tag{19}$$

We can make one more simplification if the beam parameters lie within a reasonable range. Given our input parameters $w \sim 1.5$ mm, $f_1 \sim 400$ mm, and $\lambda \sim 670$ nm, we observe that $\pi w^2 \sim 5$ mm^2 while $\lambda f_1 \sim 0.27$ mm^2; therefore, $(\pi w^2)^2 >> (\lambda f_1)^2$ by a factor of 700, which allows us to drop the $(\lambda f_1)^2$ term in Eq. (19), obtaining $\alpha = \lambda f_1^2/\pi w^2$, as given in Eq. (3).

Appendix B: Algorithm for calculation of focusing through uniaxial crystals

Here we provide an algorithm for calculating the effect of propagating a focusing beam through a birefringent crystal using standard ray-tracing. We first determine what percentage of an incident beam with a given polarization propagates as extraordinary light, and what fraction as ordinary light. We then calculate how a single ray traces through a single uniaxial crystal, and finally determine the net effect on a focusing beam.

B.1 Power ratio of two eigenmodes for single ray

Given an input k-vector of polarization H or V incident at a polar angle θ with respect to the optic axis, one can calculate the ratio of energy behaving as e-rays versus o-rays. The polarization vector of the o-ray component is given by $\overline{E_o} = \left[\left(\overrightarrow{OA} \times \vec{k}\right) \bullet \vec{E}\right]\left(\overrightarrow{OA} \times \vec{k}\right)$, and the polarization vector of the e-ray component must then be $\overline{E_e} = \vec{E} - \overline{E_o}$. Thus, we obtain the power ratio between the o-ray and e-ray components for a given input ray: $A_o / A_e = \left|\overline{E_o}\right|^2 / \left|\overline{E_e}\right|^2$. This calculation shows that as the optic axis approaches the propagation axis, an incident H or V beam no longer corresponds to ordinary and extraordinary, but rather a mixture of each. As stated above, in this case the system's eigenmodes are radially and azimuthally polarized beams.

B.2 Propagation of single ray through a uniaxial crystal

In order to calculate shifts in x, y, and z of the focal location of a given o- or e-ray after propagation through a given set of uniaxial crystals, it often suffices to trace a single ray through a single crystal. One can obtain a more exact result by tracing multiple rays with this algorithm.
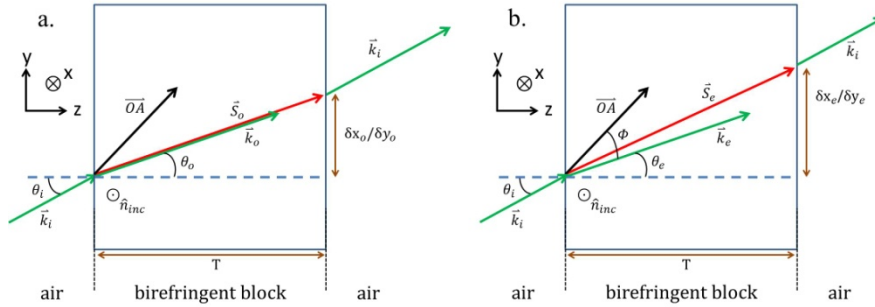

Fig. 12. Propagation of the o-wave (a) and e-wave (b).

First, we define the optic axis to be in y-z plane at angle Φ from the z axis, as in Fig. 12(b). We then separate our problem into two parts, the o-ray and e-ray component; the final output could be found by considering the power ratio found in Subsection B.1. To calculate the o-wave propagation focal shifts, we simply apply Snell's law, $\theta_o = \arcsin[n_{air}/n_o \sin(\theta_i)]$. Because the ordinary beam does not experience walk-off, simple trigonometry gives the transverse shifts $\delta x_o = dk_x^o / k_z^o$ and $\delta y_o = dk_y^o / k_z^o$.

To trace the e-ray's path, we must also take into account both spatial walk-off and angle-dependent index of refraction. Snell's law then gives $\theta_e = \arcsin[n_{air}/n_{eff} \sin(\theta_i)]$. However, the e-ray now has an index of refraction $n_{eff} = \{[\sin(\Phi)/n_e]^2 + [\cos(\Phi)/n_o]^2\}^{-1/2}$ which depends on the angle $\Phi = \arccos[(\vec{k}_e \bullet \overrightarrow{OA}) / (|\vec{k}_e||\overrightarrow{OA}|)]$ between the e-ray k-vector and the optic axis. Solving for θ_o, and therefore k_e, thus requires numerically solving a transcendental equation.
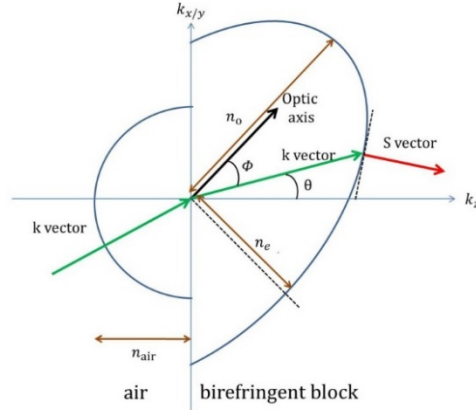
Fig. 13. Schematic of k-surfaces [25].

After refracting into the crystal, e-rays experience walk-off, and travel in the direction of the Poynting vector S, which is proportional to the gradient of the k-ellipsoid (at the point where the extension of $\vec{k}_e$ pierces the ellipsoid) [25]. Thus, we can obtain the ray direction S by finding the intersection point of a line with slope $\vec{k}_e$ and the k-ellipsoid (which is specified by the optic axis orientation), as in Fig. 13, and then calculating the local gradient of the k-ellipsoid. Finally, propagating S through the crystal by trigonometry gives the transverse walk-offs $\delta x_e = dS_x^e/S_z^e$ and $\delta y_e = dS_y^e/S_z^e$. Thus far, we have merely calculated the positional shift of a single ray in traveling through a uniaxial crystal.
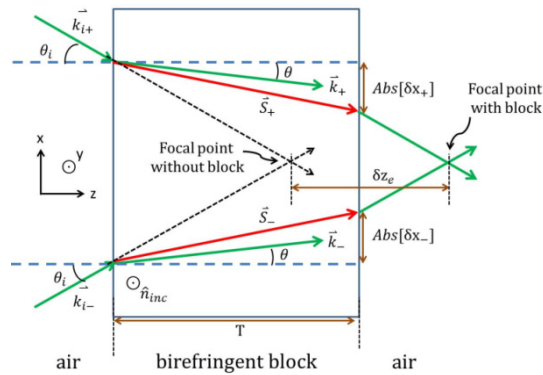
B.3 Net effect on focusing beam

Fig. 14. Schematic for focal plane displacement of the top- and bottom-most e-rays in the x-z plane. The schematics for e-rays in the y-z plane, and for o-rays in both planes, are similar.

We can now find the distance between e-ray and o-ray focal planes in a focusing beam. The calculation is simplified by assuming the focusing beam is enveloped by the two outermost rays along both x and y, and the focal plane is at their intersection. (An exact calculation can be done with the algorithm above, but exact models using Zemax ray-tracing software validate the above assumption.) Thus, we consider the outer pairs of rays within the focusing cone of rays for both H and V in the x- and y- directions. This total of 8 rays will give 4 focal locations. Here we consider only one pair; other pairs of rays behave similarly, except that for o-rays, the k-vector and Poynting vector in Fig. 14 are collinear.

To see how one pair of rays behaves, consider an extraordinary ray with polarization H and traveling in the x-z plane. The focus is where the rays meet (Fig. 14); thus, we can trigonometrically calculate the displacement of the focus in the direction of propagation:

$$\delta z = T - \frac{\text{Abs}[\delta x_+ - \delta x_-]}{2w/f}, \qquad (20)$$

where the plus (minus) sign denotes the top (bottom) incident rays, f is the lens focal length, and w is the beam waist incident on the lens. Note that δz is now defined as the distance from the focal plane *after the crystal* to where the focal plane *would have been* if focusing in free space. This convention (different from that in our paper) allows the calculation to be done generally and for each pair of rays independently. For rays in the y-z plane, we find the focal displacement along the z-axis $\delta z = T - \text{Abs}[\delta y_+ - \delta y_-]f/2w$ and focal displacements along the x- and y-axis of $\delta x = \text{Abs}[\delta x_+ + \delta x_-]/2$ and $\delta y = \text{Abs}[\delta y_+ + \delta y_-]/2$ respectively.

One can now calculate the effect of focusing through a given set of uniaxial crystals. For any specific ray, one first calculates δx_e, δx_o, δy_e, and δy_o, the transverse distances traveled by the ray *within* the block, and from this computes the final focal location in three dimensions with respect to their free-space location using the above formulas. If only the relative positions of the extraordinary/ordinary focus are required (as in our PDF schemes), then focal separations (given by the symbol Δ) in our paper's main body are found simply by subtraction.

Acknowledgments